

# Small-Signal Modelling and Design Validation of PV-Controllers with INC-MPPT using CHIL

Mandip Pokharel, *Student member, IEEE*, Avishek Ghosh, *Student member, IEEE*, and Carl Ngai Man Ho, *Senior Member, IEEE*

**Abstract**—The maximum energy that can be harvested from a photovoltaic (PV) system at any instant depends on the effectiveness and response time of the maximum power point tracking (MPPT) algorithm used and related controllers. To facilitate proper controller design, a precise mathematical model of the system is required. This paper presents a comprehensive small signal model capable of describing the dynamics of the power stage and controllers. The power stage consists of a PV system and a DC-DC boost converter including the parasitic elements operating in inverse-buck mode. The MPPT and PV voltage controller constitute the control system. The steady state and transient responses of the system are evaluated by Controller-Hardware-in-the-Loop (CHIL) approach where the power stage is simulated in a Real Time Digital Simulator (RTDS) and the control operations are performed in a Digital Signal Processor (DSP). The frequency response is experimentally determined using a Gain-Phase analyzer. This unique approach allows a control system designer to test and validate a control system design before implementing it with a laboratory scale hardware or any real-life application. This method adds an extra layer of design authentication on top of conventional offline simulations.

**Index Terms**—Solar Energy, Photovoltaics, Small Signal Model, Control, MPPT, Hardware-in-the-Loop, DC optimizer.

## I. INTRODUCTION

THE use of photovoltaic (PV) source as a backup supply for supporting the main power units as well as in emergency facilities has been popular over the years [1]. In addition, PV systems being renewable source are preferred in standalone and grid-connected configurations. Each PV application demands different implementation schemes. Grid connected PV systems require either a centralized inverter or multiple inverters for power transfer. This can be achieved through single or two stages. Each of these schemes have their own pros and cons [2]. The single stage topology in which a centralized inverter is responsible for Maximum Power Point Tracking (MPPT), grid current control and voltage amplification is simple and cost effective but has potential drawbacks [3]. The reduced tracking efficiency during partial shading due to centralized MPPT, losses due to module mismatch and derating result in low power output. There are other schemes where a string of PV modules interfaced with a string inverter has higher tracking efficiency as compared with the centralized inverter configuration due to localized MPPT in individual strings. Few other single stage

topologies require the PV voltage to be higher or equal to the peak of grid voltage and hence offer lesser flexibility [2]. Considering the limitations of single stage topologies, dual stage PV energy conversion techniques were introduced to obtain better flexibility in terms of mass production and higher efficiency in the energy conversion process [4]. In these topologies, each PV module or string is connected with a DC-DC converter stage that is interfaced with a DC link of a common inverter stage. While each DC-DC converter is responsible for MPPT, the DC-AC inverter takes care of the grid current and DC bus voltage control [5]. A better control is achieved on individual PV strings by implementation of distributed level energy converters, which sometimes are also referred as DC power optimizers. This approach overcomes the shortcomings of the central inverters in terms of energy harvesting efficiency, reliability as well as flexibility in operation and future enlargements.

The advantages and flexibility of using DC power optimizers under various application scenarios are discussed in [6]. A high gain DC-DC converter-based power optimizer is proposed in [5] that helps achieve an accurate MPPT and higher energy conversion efficiency. MPPT in the DC power conversion stage may be achieved using different topologies; [7] uses interleaved boost converter while [8] uses SEPIC converter to perform the MPPT. There are no such limitations in the topology itself and are also application dependent. The limitations are rather with the controller or the control algorithm as the same topology may exhibit improved power conversion and MPPT efficiency with use of more advanced algorithms [9], [10]. The selection of control algorithms also depends on the system design requirements.

Fig. 1 shows a grid connected DC optimizer with distributed DC MPPT tracking cells. Each of these cells are sometimes referred as Micro Boost Cell (MBC) [11]. The MBC typically consists of a boost converter connected with PV source on one end and a DC bus at the other end. The task of the controller is to track the Maximum Power Point (MPP) as well as to maintain PV voltage at MPP.

In this paper, a simplified approach to obtain the comprehensive small signal model of a MBC is proposed. This model enables robust and accurate control system design and evaluation of system performance. The small signal model consists of a linearized model of PV, an outer loop responsible

---

This work was supported in part by a grant from the NSERC Discovery Grants program, Canada (Sponsor ID: RGPIN-2016-05952).

M. Pokharel, A. Ghosh, and C. Ho are with the RIGA Lab, Department of Electrical and Computer Engineering, University of Manitoba, Winnipeg, MB, R3T 5V6, Canada, (e-mail: pokharem@myumanitoba.ca, ghosha3@myumanitoba.ca, carl.ho@umanitoba.ca).

for MPPT and an internal voltage control loop. The small signal model of a controller implemented in a Digital Signal Processor (DSP) is verified with a real-time simulator-based testing environment. The power stage consisting of a PV source and a boost converter is simulated in RSCAD, which is a Real Time Digital Simulator (RTDS) based interfacing software. The controller is implemented using a F28M35 TI DSP, which is commonly used in industry. This method of implementation is widely known as Controller-Hardware-in-the-Loop (CHIL) [12]. In addition to development of the small signal model, this paper proposes an unique approach of frequency response measurement using a Gain-Phase analyzer by further extending the CHIL implementation.

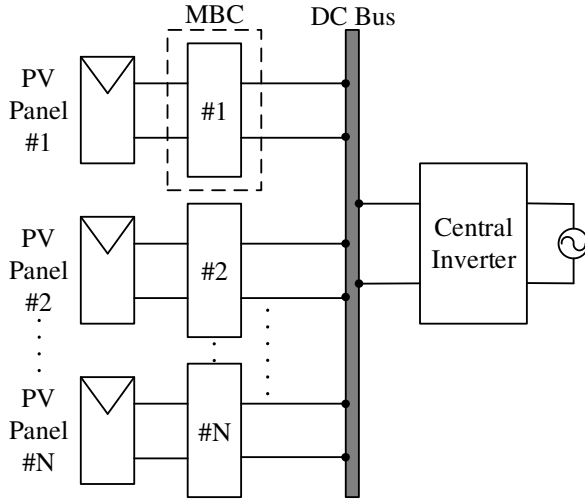


Fig. 1. A DC optimizer with Micro Boost Cell (MBC)

In control system design and optimization studies, the model and controller are conventionally validated by simulations as well as with laboratory-scale hardware setups [13]. However, the proposed system-evaluation approach allows a control system designer to test and ensure the robustness of the controller in an environment that closely emulates its real-world application. This technique offers great flexibility in design process and scalability, as it allows easy change of design parameters to study the system response.

The rest of the paper is organised in the following way; the topology of the power stage and the MPPT control technique are introduced in Section II. The mathematical modelling of PV source, PWM modulator, MPPT and voltage controller, and boost converter is discussed in Section III. Section IV describes the methodology used to design the control system by studying the frequency response using transfer functions derived in the previous sections. The experimental setup with interfacing of power stage in RTDS and controller in DSP is described in Section V along with presentation of experimental results. The closed loop frequency responses obtained using Gain-Phase analyzer, Bode100 is analysed by drawing comparison with mathematical modelling and simulation results.

## II. SYSTEM ARCHITECTURE

The system consists of a PV panel connected to a boost converter controlled through a digital controller at MPP.

Among other DC-DC converters, boost is considered efficient as well as flexible in terms of stepping up the panel voltage by significant amount [14]. In the first stage a small signal model of the converter and their controllers is developed followed by their validation. The system is further analyzed in the entire range of I-V curve to demonstrate its performance along various operating points.

### A. Topology of MBC

Fig. 2 shows schematic of a typical MBC. A boost converter coupled to a PV source constitutes the power conversion stage whereas a MPPT and voltage controller forms the controller stage in a typical MBC. The power exchange occurs between the DC grid and the PV source. A constant DC voltage source  $v_{dc}$  is connected at the output terminal of the boost converter to represent the DC bus of the DC optimizer shown in Fig.1 [15]. Although the topology is same as a simple boost converter, the principle of operation is different. The output voltage is fixed by the central inverter as shown in Fig. 1. The boost converter in this application is used to control the input voltage in contrast to the output voltage control of a conventional boost converter. This difference makes the state space model of the power circuit different from that of a simple boost converter.

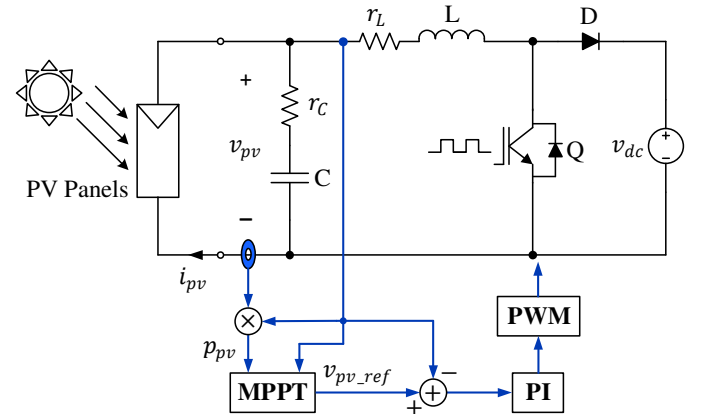


Fig. 2. A typical scheme of MBC

### B. Control Strategy

There are two control loops associated with a MBC in Fig. 2. In the first loop of MPPT, the Incremental Conductance (INC) algorithm is used to track the PV panel voltage at MPP under different operating conditions. The measurement of PV panel voltage  $v_{pv}$  and current  $i_{pv}$  is required to track the instantaneous power  $p_{pv}$ . Based on the INC algorithm, any deviation from the MPP would result in the change in conductance estimated through the computation of derivative of instantaneous power with respect to voltage i.e.  $dp_{pv}/dv_{pv}$ . The point at which this ratio becomes zero is the point of MPP and the corresponding voltage at this point is considered by the MPPT controller as the reference voltage  $v_{pv\_ref}$ . This reference voltage is fed to the inner control loop in which the Proportional Integral (PI) controller tries to maintain the input voltage at  $v_{pv\_ref}$ . To reiterate, even though the topology of power circuit is a boost converter, its principle of operation is similar to that of a typical buck converter hence it is often referred as inverse buck converter [16].

### III. MATHEMATICAL MODELLING

#### A. Linearized Model of PV

The PV source can be linearized around the MPP by a tangent passing through the MPP. The typical I-V characteristics of a PV panel is shown in Fig. 3 and a point  $(V_{mpp}, I_{mpp})$  is marked in the curve to indicate the MPP. A tangent drawn at this point with a slope  $-1/R_{mpp}$  represents the conductance of the system ( $R_{mpp}$  being the resistance of the system at MPP). Henceforth the linear model of PV operating at its MPP is represented with a negative resistive source [17].

Mathematically, it can be expressed as a linear equation having a certain slope.

$$i_{pv} - I_{mpp} = -\frac{1}{R_{mpp}} \cdot (v_{pv} - V_{mpp}) \quad (1)$$

The above equation can be readily used to represent the linear model of a PV source operating around the point of MPP. This equation is valid as long as the system operates around the MPP and is therefore helpful to develop the small signal model of PV source with MPPT.

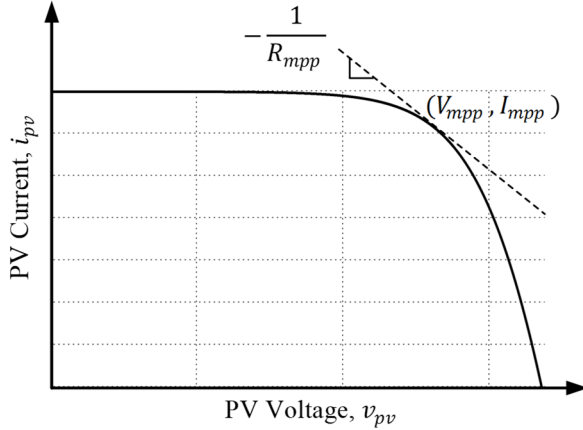


Fig. 3. Linear model of PV source

If the linear model of PV is to be operated at points other than MPP, expression (1) cannot guarantee the accuracy. Therefore, one of the approach to develop the linear PV model is to linearize the PV equation about the operating points. The Single-Diode (SD) model is considered in this paper to validate the PV model at points other than MPP. There are other improved models in literatures which considers the accuracy in developing the PV model [18],[19]. Similarly,[20] discusses on developing the dynamic model of the PV considering both the forward and reverse bias characteristics of diode, parallel capacitances and series inductances. All these models have their own advantages in terms of accuracy or completeness. Moreover, the SD model in [21],[22] offers a fair balance between accuracy and simplicity and hence the similar model has been chosen in this paper for analysis. The SD model presented in [22] can be represented by the mathematical expression in (2). Linearizing (2) about an operating point gives the conductance at that particular point.

$$i_{pv} = I_{pv} - I_o \left[ e^{\left( \frac{v_{pv} + R_s i_{pv}}{V_t N_s a} \right)} - 1 \right] - \frac{v_{pv} + R_s i_{pv}}{R_p} \quad (2)$$

Differentiating (2) about any operating point  $(V, I)$  the conductance may be estimated [22]. The equation governing the conductance can be expressed as;

$$g(V, I) = \frac{-I_o \cdot e^{\left( \frac{V + I R_s}{N_s V_t a} \right)} - \frac{1}{R_p}}{1 + \frac{R_s}{R_p} + I_o \cdot e^{\left( \frac{V + I R_s}{N_s V_t a} \right)} \cdot \frac{R_s}{N_s V_t a}} \quad (3)$$

where,  $I_{pv}$  and  $I_o$  are the photovoltaic and saturation currents of the array and  $V_t$  is the thermal voltage of the array with  $N_s$  cells connected in series.  $R_s$  and  $R_p$  are the equivalent series and parallel resistance of the array.  $a$  is the diode ideality constant.

#### B. Mathematical Model of Power Circuit

For the completeness of modelling, the boost converter is modelled with parasitic resistances of both inductor and capacitor. The inclusion of parasitics in the power stage simplifies the controller design, as the damping introduced by these parasitic elements eliminates the need for an additional differential component and just a standard PI controller can maintain the PV array voltage at the reference [23].

The schematic in Fig. 4 consists of a linear model of PV represented with a resistance  $R_{mpp}$  and a boost converter including the parasitic resistances  $r_L$  and  $r_C$  associated with the inductor  $L$  and capacitor  $C$  respectively. The state space averaging technique is used to represent the converter in terms of its low frequency small signal transfer function.

There are two operating modes due to the switching of main semiconductor switch Q in Fig. 4; Q=ON represented by Mode I when switch position is in "1" and Q=OFF represented by Mode II when switch position is in "2". State equations for each operating mode are averaged to combine them using the duty cycle information. The converter is assumed to be operating in continuous conduction mode (CCM) and the natural frequency of the converter is much lower than the switching frequency [24], [25].

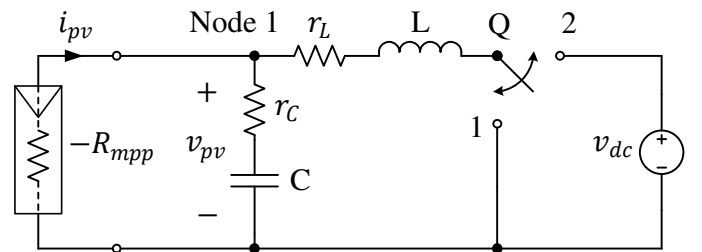


Fig. 4. Physical representation of power conversion stage

Using the following definitions to operating circuit in Fig. 4,

- State variables  $x(t)$  as inductor current and capacitor voltage;  $x(t) = \{i_L(t), v_C(t)\}$ .
- Input variable  $u(t)$  as the DC link voltage  $v_{dc}$ .
- Output variable  $y(t)$  as the PV voltage  $v_{pv}(t)$ .

For Mode I operation with Q=ON, the state equations are,

$$\frac{dv_C}{dt} = -\frac{R_{mpp}}{C(R_{mpp} + r_C)} \cdot i_L - \frac{1}{C(R_{mpp} + r_C)} \cdot v_C \quad (4)$$

$$\frac{di_L}{dt} = -\frac{R_{mpp}(r_C + r_L) + r_L r_C}{L(R_{mpp} + r_C)} \cdot i_L + \frac{R_{mpp}}{L(R_{mpp} + r_C)} \cdot v_C \quad (5)$$

An expression for the output in terms of state variables can be derived as,

$$v_{pv} = -\frac{r_c R_{mpp}}{(R_{mpp} + r_c)} \cdot i_L + \frac{R_{mpp}}{(R_{mpp} + r_c)} \cdot v_c \quad (6)$$

For Mode II operation with Q=OFF, the state equation of (4) remains valid for this mode as well. The state equation with respect to  $i_L(t)$  however changes.

$$\frac{di_L}{dt} = -\frac{R_{mpp}(r_c + r_L) + r_L r_c}{L(R_{mpp} + r_c)} \cdot i_L + \frac{R_{mpp}}{L(R_{mpp} + r_c)} \cdot v_c - \frac{v_{dc}}{L} \quad (7)$$

A detailed derivation of (4) – (7) is presented in the Appendix.

Comparing the state and output equations with the standard averaged state equation, the respective state, input and output matrices can be easily extracted. The averaged state equations are given by:

$$\begin{aligned} \dot{x} &= [A]x + [B]u \\ y &= [C]x \end{aligned} \quad (8)$$

where,  $A = A_1 d + A_2(1 - d)$ ,  $B = B_1 d + B_2(1 - d)$ ,  $C = C_1 d + C_2(1 - d)$  and  $d$  the duty cycle. The ON time is defined by  $dT_s$  and OFF time by  $(1 - d)T_s$ , where  $T_s$  is the time period for one switching cycle.

Comparing (4), (5), (6) and (7) with the standard averaged state equations (8),

$$A = A_1 = A_2 = \begin{bmatrix} -\frac{R_{mpp}(r_c + r_L) + r_L r_c}{L(R_{mpp} + r_c)} & \frac{R_{mpp}}{L(R_{mpp} + r_c)} \\ -\frac{R_{mpp}}{C(R_{mpp} + r_c)} & -\frac{1}{C(R_{mpp} + r_c)} \end{bmatrix}$$

$$B_1 = \begin{bmatrix} 0 \\ 0 \end{bmatrix}; B_2 = \begin{bmatrix} -\frac{1}{L} \\ 0 \end{bmatrix}; C = C_1 = C_2 = \begin{bmatrix} -\frac{r_c R_{mpp}}{R_{mpp} + r_c} & \frac{R_{mpp}}{R_{mpp} + r_c} \end{bmatrix}$$

Introducing small signal perturbation in state variables and duty cycle and taking Laplace transform, the power-stage transfer function can be determined as:

$$T_p(s) = \frac{\tilde{v}_{pv}}{\tilde{d}} = C \cdot [sI - A]^{-1} \cdot [(A_1 - A_2) \cdot X + (B_1 - B_2) \cdot V_{dc}] + (C_1 - C_2) \cdot X \quad (9)$$

By substituting values of  $A_1, A_2, B_1, B_2, C_1$  and  $C_2$  into (9):

$$T_p(s) = \frac{-V_{dc}}{L} \cdot \left\{ \frac{R_{mpp}^2}{C \cdot R_{C\_mpp}^2} + \frac{r_c \cdot R_{mpp} \left( s + \frac{1}{C \cdot R_{C\_mpp}} \right)}{R_{C\_mpp}} \right\} \cdot \frac{1}{p(s)} \quad (10)$$

where,  $R_{C\_mpp} = r_c + R_{mpp}$  and

$$p(s) = \frac{R_{mpp}^2}{L \cdot C \cdot R_{C\_mpp}^2} + \left( s + \frac{1}{C \cdot R_{C\_mpp}} \right) \left( s + \frac{r_c \cdot R_{mpp} + r_L \cdot R_{C\_mpp}}{R_{C\_mpp}} \right)$$

With the small signal transfer function of power stage developed, the mathematical models of MPPT and voltage controller is required to complete the small signal model of the overall system shown in Fig. 2.

### C. Mathematical Model of MPPT Controller

The input to MPPT controller is PV voltage and current, which is used to generate the reference voltage at which the instantaneous power from the PV array is maximum. The operating point can be easily estimated based on the

incremental conductance computed by calculating  $\Delta p_{pv}/\Delta v_{pv}$ . Mathematically, INC may be expressed as:

$$\begin{aligned} \frac{dp_{pv}}{dv_{pv}} &= \frac{d(v_{pv} \times i_{pv})}{dv_{pv}} = i_{pv} + v_{pv} \cdot \frac{di_{pv}}{dv_{pv}} \Rightarrow \frac{1}{v_{pv}} \cdot \frac{dp_{pv}}{dv_{pv}} = \frac{i_{pv}}{v_{pv}} + \frac{di_{pv}}{dv_{pv}} \\ \Rightarrow e &= \frac{i_{pv}}{v_{pv}} + \frac{di_{pv}}{dv_{pv}} \end{aligned} \quad (11)$$

In (11), the error  $e$  is expressed as a sum of the actual conductance  $i_{pv}/v_{pv}$  and the incremental conductance  $di_{pv}/dv_{pv}$ . The maximum power can be harvested from the PV array at the point where the measure of incremental and actual conductance is equal. If this ratio is greater than zero, the operating point lies to the left of MPP and it lies to the right if this ratio is less than zero, as shown in Fig. 5.

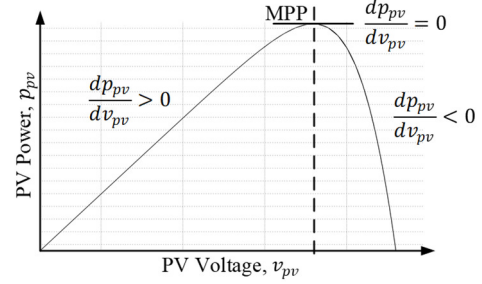


Fig. 5. Graphical representation of INC algorithm

Linearizing (11) around MPP ( $V_{mpp}, I_{mpp}$ ) as shown in Fig. 3 and Fig. 5. The small signal model is,

$$\tilde{e} = K_m \cdot \tilde{v}_{pv} \quad (12)$$

where,  $K_m = -\frac{2}{R_{mpp} \cdot V_{mpp}}$

A detailed derivation of (12) is included in the Appendix.

The above equation gives the small signal relation between error variable  $\tilde{e}$  and PV voltage  $\tilde{v}_{pv}$  with a factor  $K_m$  that describes the MPPT action. This error when fed through an integrator generates the required voltage reference. Mathematically, this may be shown by,

$$V_{pv\_ref}[k] = V_{pv\_ref}[k - 1] + K_i \cdot \frac{T_s}{2} (E[k] + E[k - 1]) \quad (13)$$

A detailed derivation of (13) is shown in the Appendix.

Since the implementation is carried out digitally, discrete integrator is considered for the entirety of the modelling. (13) gives the expression for digital implementation of an integrator. This discrete integrator of trapezoidal form is then converted to its s-domain continuous time counterpart using the bilinear Tustin's transformation for modelling purpose. This would simply result in  $K_i/s$ .

### D. Voltage Controller and PWM modulator

A PI controller may be used to control the process consisting of power stage and PWM modulator. The transfer function of a typical PI controller is given below in (14). Since the overall open loop gain of the voltage control loop is negative, the PI controller is designed with a negative component such that a positive gain is finally introduced in the system.

$$T_c(s) = -\left( \frac{K_p s + K_i}{s} \right) \quad (14)$$

The PI controller above is digitally implemented in DSP to regulate the PV voltage at its reference MPP value. The digital implementation of PI controller requires the z-transform of the continuous-time function of PI controller.

$$v_i[k] = v_i[k-1] + r[k] \cdot \left[ K_p + \frac{K_i T_s}{2} \right] + r[k-1] \cdot \left[ \frac{K_i T_s}{2} - K_p \right] \quad (15)$$

A detailed derivation of (15) is presented in the Appendix.

With the mathematical model developed in digital platform, the discrete model of the PWM modulator can then be developed. From Fig. 6, the small signal transfer function of the PWM modulator can be expressed as:

$$T_m(s) = \frac{\tilde{d}(s)}{\tilde{v}_i(s)} = \frac{1}{\tilde{V}_r} \quad (16)$$

where,  $v_i(t)$  is the input signal of the modulator and  $\tilde{V}_r$  is the peak value of the carrier. A detailed derivation of (16) is included in the Appendix.

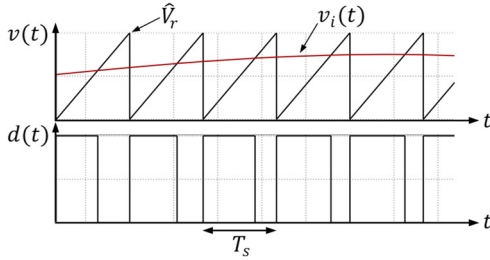


Fig. 6. Generation of PWM signal

From (16) it is seen that the transfer function of the PWM modulator is a gain expressed as the reciprocal of the carrier-peak.

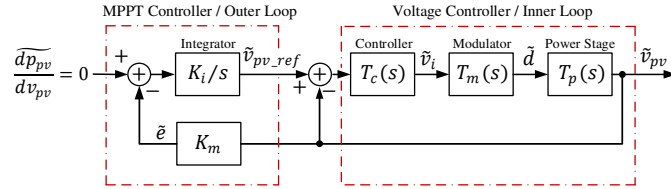


Fig. 7. Comprehensive small signal model of PV source with MPPT

With the mathematical models for power stage, MPPT controller, voltage controller and PWM modulator, the small signal relationship between these key elements are represented with a block diagram in Fig. 7.

#### IV. SYSTEM VALIDATION AND CONTROLLER DESIGN

##### A. MBC Model Validation

The mathematical model of MBC presented in Section III is validated in the entire region of the I-V curve considering a single BP-365 PV-module. The specification of the module is presented in TABLE I.

The model proposed in Section III is validated in the constant current (CC) region, MPP and constant voltage (CV) region of the I-V curve. In this model, the PV source is modelled as a negative resistance. It may be noted that the value of this resistance changes for every operating point. The linearized PV model given by equation (3) is used to calculate

the equivalent PV resistance for that point. The key parameters for this model is determined in a similar way shown in [22] and is tabulated in TABLE II.

TABLE I PARAMETERS OF BP 365 PV MODULE AT STC

PV Module Parameter	Value
Open circuit Voltage ( $V_{OC}$ )	22.1 V
Short circuit current ( $I_{SC}$ )	3.99 A
Voltage at MPP ( $V_{mpp}$ )	17.6 V
Current at MPP ( $I_{mpp}$ )	3.69 A
Power at MPP ( $P_{max}$ )	65 W
Temperature coefficient of $I_{SC}$	0.065 %/°C
Temperature coefficient of $V_{OC}$	-0.08 V/°C

In Fig. 4,  $R_{mpp}$  is replaced with the corresponding resistances at each operating point while performing the analysis. The AC sweep results from PLECS are superimposed with the mathematical model frequency response for each of these points and is presented in Fig. 8.

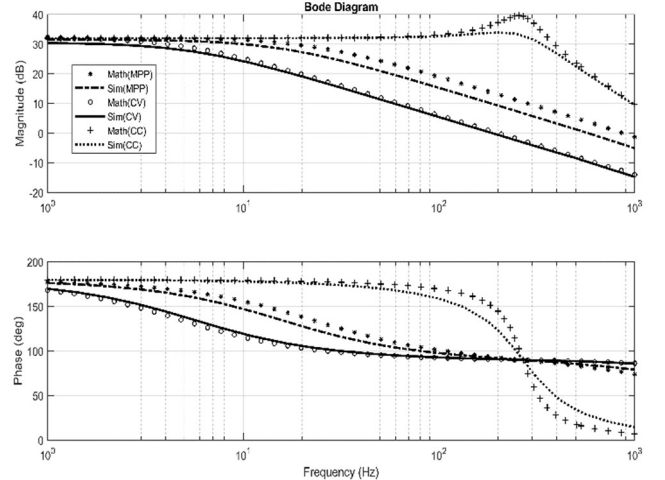


Fig. 8. Power stage frequency response at different points in I-V curve

TABLE II EQUIVALENT SINGLE DIODE MODEL DATA FOR BP 365

Parameter	Value
Saturation Current ( $I_0$ )	7.4198e-10 A
Series Resistance ( $R_S$ )	0.444 $\Omega$
Parallel Resistance ( $R_P$ )	204.027 $\Omega$
Ideality Factor (a)	1.067

Both the results exhibit a close match thus validating the small signal model derived for the power stage. Also, the model accuracy is investigated through frequency response for variation in input capacitance considering the stray capacitance contributed by the PV string. The model showed a very little to no variation in gain and phase from original specified capacitance.

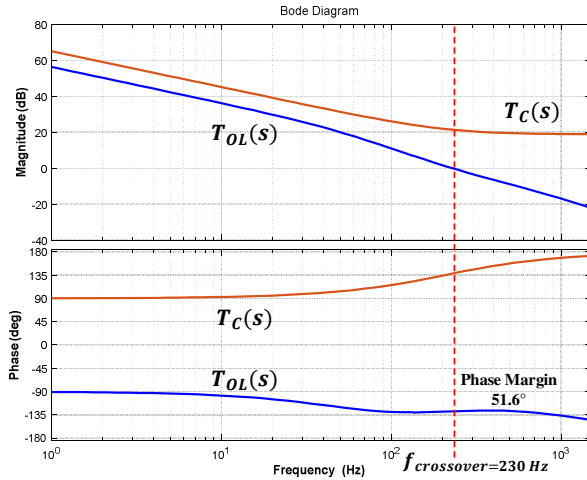
Once the model is validated with single PV module, it is scaled up to  $10 \times 4$  array system with specifications shown in TABLE III for implementation purpose.

TABLE III SYSTEM SPECIFICATION

PV Source Parameter	Value	Converter Parameter	Value
Rated power	2.6 kW	Output Voltage	400 V
Open Circuit Voltage ( $V_{oc}$ )	221 V	Input Capacitance	10 $\mu$ F
Voltage at MPP ( $V_{mpp}$ )	176 V	Capacitive resistance	0.05 $\Omega$
Short Circuit current ( $I_{sc}$ )	15.96 A	Inductor	35 mH
Current at MPP ( $I_{mpp}$ )	14.76 A	Inductive resistance	0.2 $\Omega$
Array Size	10 X 4	Switching Frequency	2 kHz

### B. Controller Design

The inner control loop constitutes the process to be controlled i.e. boost converter power stage coupled with PV source (modelled as impedance) and PWM modulator. Whereas the MPPT controller represents the outer loop which generates a voltage reference for the inner loop. With the transfer functions derived in the previous section and system specification shown in TABLE III, the frequency responses of the overall open loop transfer function  $T_{OL}(s)$  is studied to design a suitable error amp for the inner loop. The selection of controller parameters and appropriate bandwidth is done by studying the frequency response of the inner loop (power stage, PWM modulator and controller) shown in Fig. 9.

Fig. 9. Frequency response of inner loop  $T_{OL}(s)$  and controller  $T_C(s)$ .

The overall open loop transfer function of the voltage control loop is given by:

$$T_{OL}(s) = T_C(s) \cdot T_m(s) \cdot T_p(s) \quad (17)$$

The frequency response of  $T_{OL}(s)$  is plotted using transfer functions of  $T_p(s)$ ,  $T_C(s)$  and  $T_m(s)$  from (10), (14) and (16) respectively.

As a rule of thumb, the bandwidth of the inner loop is designed at approximately one-tenth of the switching frequency [26] i.e. at 230 Hz as seen from Fig. 9. A phase margin of  $51.6^\circ$  at the crossover ensures control system stability and high gain of  $T_{OL}(s)$  at low frequency minimizes the steady-state error.

The MPPT and voltage control loops are designed with different bandwidths and the controller parameters are carefully chosen to avoid any possible interference between the two loops.

### C. Controller Performance Evaluation

The response of the designed controller with the chosen MPPT algorithm is assessed for variation of operating conditions such as change in irradiance and temperature. The simulation results for the dynamically changing environmental conditions is presented in Fig. 10.

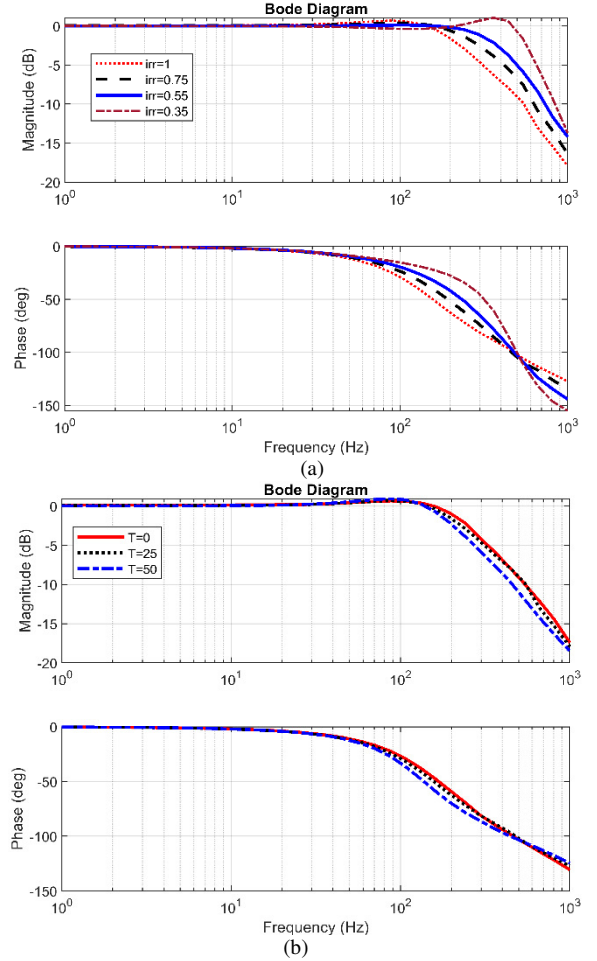


Fig. 10. Frequency response of inner loop with varying (a) Irradiance at Temp=25°C and (b) Temperature at Irradiance=1 Sun

The variation observed in the magnitude and phase plots of Fig. 10 is due to the change of the impedances between MPP points. The system response however remains similar for all operating points with respect to STC response.

Further to verify the robustness of the controller, the system is simulated with dynamic transition in irradiance causing the inductor current to switch from continuous to discontinuous conduction mode (DCM). The controller can accurately track the correct operating point even during transients, which proves its robust operation. Fig. 11 demonstrates the controller performance during the transient. The boundary current  $I_{LB}$  between CCM and DCM for boost converter can be expressed with (18), which serves as a mathematical tool for selection of current and irradiance [27].

$$I_{LB} = \frac{V_{dc}}{2 \cdot L \cdot f_{sw}} \cdot D \cdot (1 - D) \quad (18)$$

The duty cycle (D) can be calculated using steady state equations of boost converter while  $V_{dc}$ , L and  $f_{sw}$  are known from the converter specifications in TABLE III.

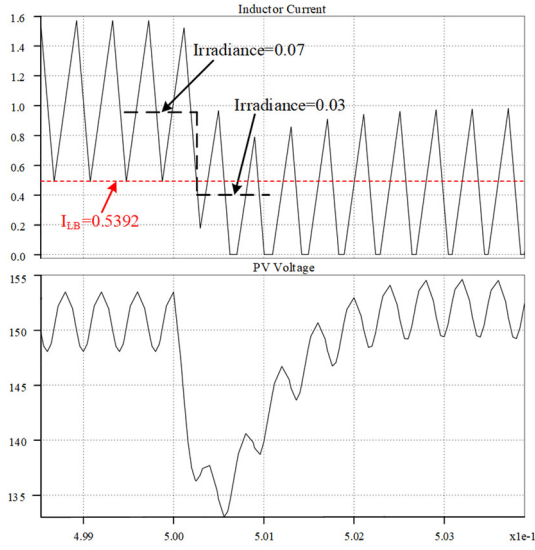


Fig. 11. Dynamic transition from CCM to DCM

Further extending the analysis, the loci of MPP operating points are plotted for different values of irradiances and temperatures in Fig. 12. At 25°C, the system moves from CCM to DCM as the inductor current falls below the boundary current with irradiance dropping below 40 W/m<sup>2</sup>. This phenomenon is also seen in the simulation result of Fig. 11. Similar behavior is noticed for other operating points in Fig. 12.

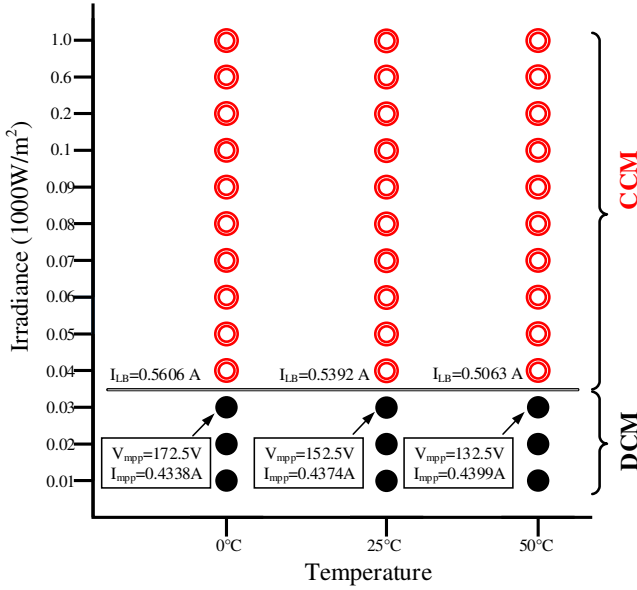


Fig. 12. Loci of operating points with variation in temperature and irradiance

## V. SYSTEM IMPLEMENTATION AND EXPERIMENTAL RESULTS

In order to study the dynamic behavior of the control loops in a practical control hardware and to verify the determined small signal models, CHIL testing methodology is used. The power stage is implemented in the RTDS simulator using RSCAD. The control loops are implemented in TI F28M35x which is a 150 MHz clock, 12-bit ADC resolution DSP with 300KHz sampled data. The PV voltage and current are sensed

using an analog interface between the DSP controller and RSCAD power stage. The analog interface consists of the Giga-Transceiver Analog Output (GTAO) card and Analog to Digital converter (ADC) of the DSP. A digital interface provides the gate pulses to the converter from the controller using Giga-Transceiver Digital Input (GTDI) card. The setup used for the experiment is shown in Fig. 13.

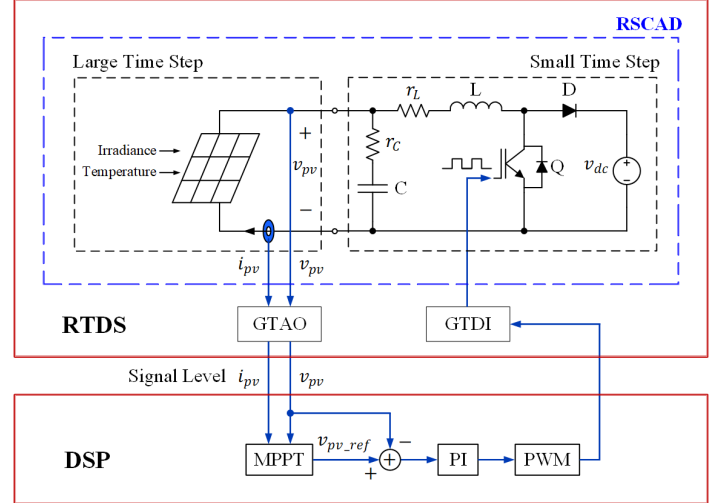


Fig. 13. CHIL implementation using RTDS and DSP

In the RSCAD environment, the PV source with specifications shown in TABLE III, is simulated in the large-time step at 30  $\mu$ s and the power stage inside the small-time step block at 1.4  $\mu$ s. The small-time step block is configured to receive the switching pulses from the GTDI card to the converter switches. The up-down counter in the DSP used as the carrier wave is set at 2 kHz, i.e. the switching frequency of the designed system. Two EPWMs running at different Interrupt Service Routine (ISR) are configured, one to perform MPPT (at 12KHz) and second to generate modulating signal (25KHz). The MPPT controller with low bandwidth filter outs the aliasing noises seen due to down sampling in this kind of multi-rate system[28]. Compare (CMP) registers are configured to store modulation signal and Action qualifier (AQ) is used to set and reset the pulses based on values in CMP registers.

The controller parameters derived in Section IV are used to experimentally verify the steady-state and transient performance of the system. Fig. 14 shows the plots for PV power, voltage and current in RSCAD runtime window. These plots are also monitored in oscilloscope and presented in Fig. 16 (a). A stable steady-state performance of the system can be observed from Fig. 14 and Fig. 16 (a). Similarly, stable performance of the system after transients are recorded in Fig. 15 and Fig. 16 (b).

To validate the small signal model of the power stage and voltage controller loop, a small signal perturbation was introduced externally in the voltage reference (MPP voltage) using a Gain-phase analyzer (Bode100) and the PV input voltage was monitored. Fig. 17 shows the detail connection along with indication of key variables measured. Since the MPPT controller block generates the reference inside the DSP, it is disabled to perform this test.

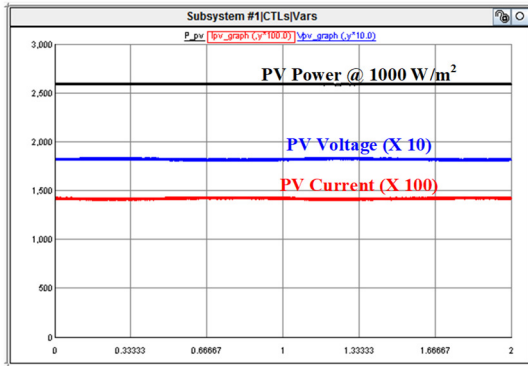


Fig. 14. Steady state response of the system captured in RSCAD runtime environment @ 1000 W/m<sup>2</sup> solar irradiance

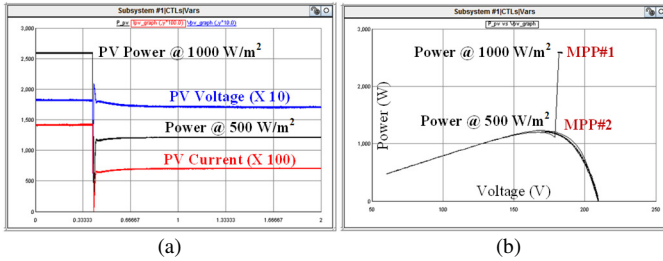


Fig. 15. (a) Transient response of the system captured in RSCAD runtime environment for solar irradiance change from 1000 W/m<sup>2</sup> to 500 W/m<sup>2</sup> (b) change of operating point in P-V curve due to transient

The frequency response obtained from Bode100 are superimposed with the frequency response of mathematical model and simulation in Fig. 18. It can be observed that the experimental results closely follow the response of the mathematical model and simulation, especially in the low frequency range. This validates the modelling of all the key elements of the inner loop from Section III as well as the controller design. It may be noted that the semiconductor switches in RSCAD are modelled as simple turn-on and turn-off resistances [29]. It is observed that the values of these resistances affect the frequency response of the system. This is a possible reason for the slight variations of the experimental results with that of the model and simulation.

## VI. CONCLUSION

In this paper, a comprehensive small signal model describing the dynamic relationship between a PV source, boost converter, INC MPPT and voltage controller have been presented. The frequency response of the system, determined using the developed small signal transfer functions, is used to compute the controller parameters. A detailed analysis showing the performance of the system during various parameter changes are studied. The models are verified and validated through simulation, mathematical analysis as well as experimental results. The experiment is conducted with real time simulation of the power stage in RTDS and control operations in DSP. A Gain-Phase analyzer is used to measure the frequency response. This approach to verify the small signal model for MBCs can provide a safe and practical testing environment to evaluate the dynamic response of a control system in actual control hardware. The simulation, experimental results showed a good agreement, which validates the mathematical models and controller design.

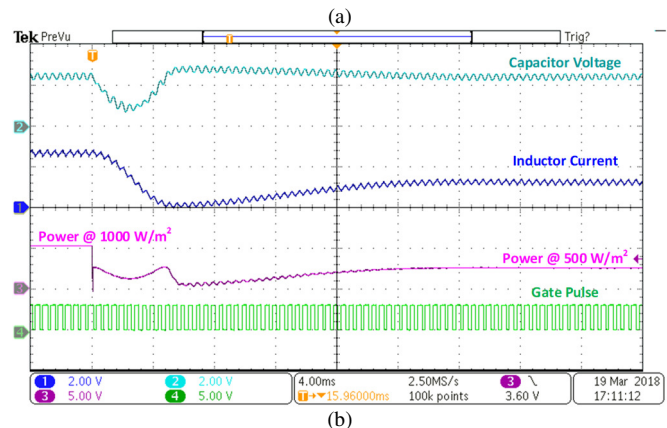
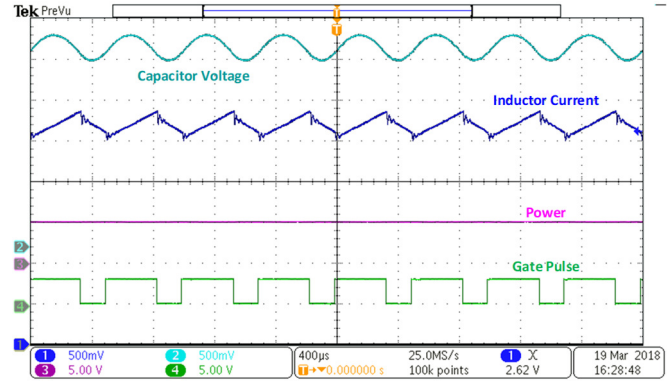


Fig. 16. Experimental evaluation of system performance (a) Steady state and (b) Transient, Ch. 1 (5 V corresponds to 26.6 A), Ch. 2 (5 V corresponds to 368.33 V), Ch. 3 (5 V corresponds to 2.597 kW)

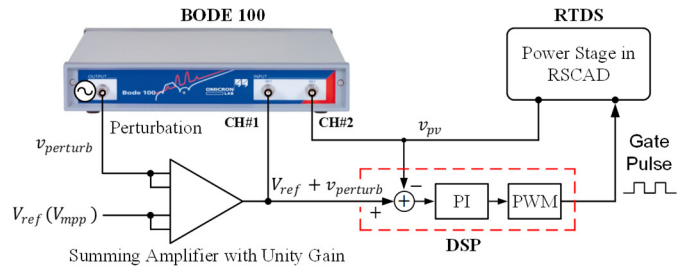


Fig. 17. Connection scheme of Bode100 for frequency response evaluation

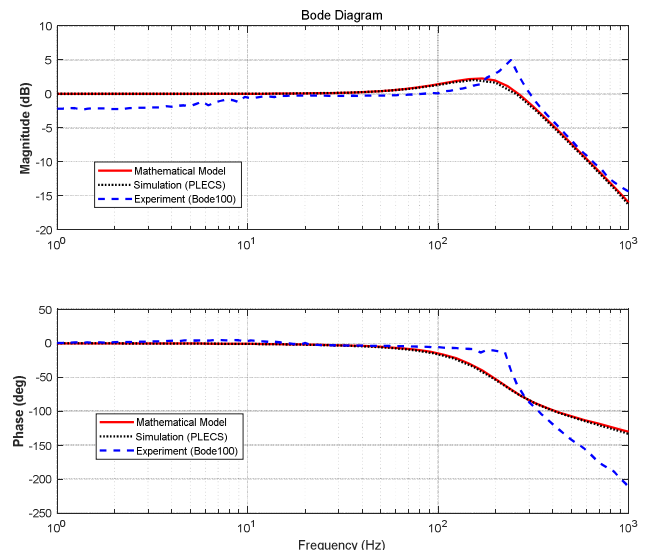


Fig. 18. Comparison of Closed loop frequency response of voltage controller from Mathematical model, Simulation and Experiment

## VII. APPENDIX

## A. Derivation of (4) – (7):

By using Kirchhoff's Voltage law (KVL) for the circuit in Fig. 4,

$$v_{pv}(t) = i_c(t) \cdot r_c + v_c(t) \quad (A1)$$

$$v_{pv}(t) = i_L(t) \cdot r_L + v_L(t) \quad (A2)$$

By using Kirchhoff's Current law (KCL) in node 1,

$$i_{pv} = i_c(t) + i_L(t) \quad (A3)$$

Using (A1), (A3) & substituting  $i_{pv}(t) = \frac{-v_{pv}(t)}{R_{mpp}}$ ;  $i_c(t) = \frac{C \cdot dv_c(t)}{dt}$ , (4) can be obtained.

Similarly, using (A1), (A2), (4) and substituting  $v_L(t) = \frac{L \cdot di_L(t)}{dt}$ , (5) can be obtained.

Substituting (4) into (A1), (6) can be obtained.

Using KVL for the circuit in Fig. 4

$$v_L(t) = v_{pv}(t) - r_L i_L(t) - v_{dc} \quad (A4)$$

Substituting (A1) and (4) in (A4), (7) can be obtained.

## B. Derivation of (12):

Using Taylor series expansion in (11):

$$e(v_{pv}, i_{pv}) = e(V_{mpp}, I_{mpp}) + \left. \frac{\partial e(v_{pv}, i_{pv})}{\partial v_{pv}} \right|_{(V_{mpp}, I_{mpp})} (v_{pv} - V_{mpp}) + \left. \frac{\partial e(v_{pv}, i_{pv})}{\partial i_{pv}} \right|_{(V_{mpp}, I_{mpp})} (i_{pv} - I_{mpp})$$

$$e(v_{pv}, i_{pv}) = -\frac{I_{mpp}}{V_{mpp}^2} (v_{pv} - V_{mpp}) + \frac{1}{V_{mpp}} (i_{pv} - I_{mpp}) \quad (A5)$$

Substituting  $i_{pv}$  from (1) into (A5),

$$e = \frac{2}{R_{mpp}} - \frac{2v_{pv}}{R_{mpp}V_{mpp}} \quad (A6)$$

Introducing small signal perturbation, (A6) is expressed as:

$$\tilde{e} = -\frac{2}{R_{mpp}V_{mpp}} \cdot \tilde{v}_{pv} \quad (A7)$$

Thus, (12) can be obtained.

## C. Derivation of (13):

A discrete integrator of trapezoidal form can be expressed as:

$$\frac{V_{pv\_ref}[z]}{E[z]} = K_i \cdot \frac{T_s}{2} \cdot \frac{z+1}{z-1} \quad (A8)$$

$$V_{pv\_ref}[z] = V_{pv\_ref}[z] \cdot z^{-1} + \frac{K_i T_s}{2} \cdot E[z] + \frac{K_i T_s}{2} \cdot E[z] \cdot z^{-1}$$

Using time shifting property (A9) on the above expression,

$$z\{x[k-n]\} = z^{-n} \cdot X[z] \text{ where, } z\{x[k]\} = X[z] \quad (A9)$$

(13) can be derived.

## D. Derivation of (15):

Taking z transform of (14):

$$T_c(z) = \frac{v_i(z)}{r(z)} = K_p + K_i \cdot \frac{T_s}{2} \cdot \frac{z+1}{z-1} \quad (A10)$$

$$v_i[z] = v_i[z] \cdot z^{-1} + K_p \cdot r[z] - K_p \cdot r[z] \cdot z^{-1} + K_i \cdot \frac{T_s}{2} \cdot r[z] + K_i \cdot \frac{T_s}{2} \cdot r[z] \cdot z^{-1} \quad (A11)$$

Using time shifting property (A9) on (A11),

$$v_i[k] = v_i[k-1] + K_p \cdot r[k] - K_p \cdot r[k-1] + K_i \cdot \frac{T_s}{2} \cdot r[k] + K_i \cdot \frac{T_s}{2} \cdot r[k-1] \quad (A12)$$

Further simplifying (A12), (15) can be obtained.

## E. Derivation of (16):

From Fig. 6, the duty cycle equation can be expressed as:

$$D(t) = \frac{v_i(t)}{\tilde{v}_r} \quad (A13)$$

Introducing small signal in (A13),

$$D + \tilde{d}(t) = \frac{v_i + \tilde{v}_i(t)}{\tilde{v}_r} \quad (A14)$$

By neglecting the DC terms in (A14), (16) is obtained.

## VIII. REFERENCES

- [1] Q. Fu, L. F. Montoya, A. Solanki, A. Nasiri, V. Bhavaraju, T. Abdallah and D. C. Yu, "Microgrid Generation Capacity Design With Renewables and Energy Storage Addressing Power Quality and Surety," *IEEE Trans. Smart Grid*, vol. 3, no. 4, pp. 2019-2027, Dec. 2012.
- [2] X. Zong, "A Single Phase Grid Connected DC/AC Inverter with Reactive Power Control for Residential PV Application," *M.S. thesis*, Univ. of Toronto, Toronto, ON, Canada, 2011.
- [3] Y. Bae and R. Y. Kim, "Suppression of Common-Mode Voltage Using a Multicentral Photovoltaic Inverter Topology With Synchronized PWM," *IEEE Trans. Ind. Electron.*, vol. 61, no. 9, pp. 4722-4733, Sept. 2014.
- [4] S. B. Kjaer, J. K. Pedersen and F. Blaabjerg, "A Review of Single-Phase Grid-Connected Inverters for Photovoltaic Modules," *IEEE Trans. Ind. Appl.*, vol. 41, no. 5, pp. 1292-1306, Sept./Oct. 2005.
- [5] S. M. Chen, T. J. Liang and K. R. Hu, "Design, Analysis, and Implementation of Solar Power Optimizer for DC Distribution System," *IEEE Trans. Power Electron.*, vol. 28, no. 4, pp. 1764-1772, April 2013.
- [6] C. Deline and S. MacAlpine, "Use conditions and efficiency measurements of DC power optimizers for photovoltaic systems," *Proc. IEEE ECCE2013*, pp. 4801-4807, 2013.
- [7] C. N. M. Ho, H. Breuninger, S. Pettersson, G. Escobar and F. Canales, "A Comparative Performance Study of an Interleaved Boost Converter Using Commercial Si and SiC Diodes for PV Applications," *IEEE Trans. Power Electron.*, vol. 28, no. 1, pp. 289-299, Jan. 2013.
- [8] M. Azab, "DC power optimizer for PV modules using SEPIC converter," *Proc. IEEE SEGE2017*, pp. 74-78, 2017.
- [9] W. M. Lin, C. M. Hong, and C.H Chen, "Neural-Network-Based MPPT Control of a Stand-Alone Hybrid Power Generation System," *IEEE Trans. Power Electron.*, vol. 26, no. 12, pp. 3571-3581, Dec. 2011.
- [10] K. Ishaque, Z. Salam, M. Amjad, and S. Mekhilef, "An Improved Particle Swarm Optimization (PSO)-Based MPPT for PV With Reduced Steady-State Oscillation," *IEEE Trans. Power Electron.*, vol. 27, no. 8, pp. 3627-3638, Aug. 2012.
- [11] S. MacAlpine and C. Deline, "Modeling Microinverters and DC Power Optimizers in PVWatts," *Tech. Rep. NREL/TP-5J00-63463*, National Renewable Energy Laboratory, Golden, Colorado, Feb. 2015.
- [12] Y. Li, D. M. Vilathgamuwa and Poh Chiang Loh, "Design, analysis, and real-time testing of a controller for multibus microgrid system," *IEEE Trans. Power Electron.*, vol. 19, no. 5, pp. 1195-1204, Sept. 2004.
- [13] H. AbdEl-Gawad and V. K. Sood, "Kalman Filter-Based Maximum Power Point Tracking for PV Energy Resources Supplying DC Microgrid," *Proc. IEEE EPEC2017*, pp. 1-8, 2017.

- [14] G. R. Walker, and P. C. Sernia, "Cascaded DC-DC Converter Connection of Photovoltaic Modules," *IEEE Trans. Power Electron.*, vol. 19, no. 4, pp. 1130-1139, July 2004.
- [15] E. Serban, F. Paz and M. Ordonez, "Improved PV Inverter Operating Range Using a Miniboost," *IEEE Trans. Power Electron.*, vol. 32, no. 11, pp. 8470-8485, Nov. 2017.
- [16] F. Paz and M. Ordonez, "High-Performance Solar MPPT Using Switching Ripple Identification Based on a Lock-In Amplifier," *IEEE Trans. Ind. Electron.*, vol. 63, no. 6, pp. 3595-3604, June 2016.
- [17] P. Manganiello, M. Ricco, G. Petrone, E. Monmasson and G. Spagnuolo, "Optimization of perturbative PV MPPT methods through online system identification," *IEEE Trans. Ind. Electron.*, vol. 61, no. 12, pp. 6812-6821, Dec. 2014.
- [18] Y. A. Mahmoud, W. Xiao and H. H. Zeineldin, "A Parameterization Approach for Enhancing PV Model Accuracy," *IEEE Trans. Ind. Electron.*, vol. 60, no. 12, pp. 5708-5716, Dec. 2013.
- [19] A. Chatterjee, A. Keyhani and D. Kapoor, "Identification of Photovoltaic Source Models," *IEEE Trans. Energy Convers.*, vol. 26, no. 3, pp. 883-889, Sept. 2011.
- [20] K. A. Kim, C. Xu, L. Jin and P. T. Krein, "A Dynamic Photovoltaic Model Incorporating Capacitive and Reverse-Bias Characteristics," *IEEE J. Photovolt.*, vol. 3, no. 4, pp. 1334-1341, Oct. 2013.
- [21] C. Carrero, J. Amador, and S. Arnaltes "A Single Procedure for Helping PV Designers to Select Silicon PV Modules and Evaluate the Loss Resistances," *Renewable Energy*, vol. 32, no. 15, 2007, pp. 2579-2589.
- [22] M. G. Villalva, J. R. Gazoli and E. R. Filho, "Comprehensive Approach to Modeling and Simulation of Photovoltaic Arrays," *IEEE Trans. Power Electron.*, vol. 24, no. 5, pp. 1198-1208, May 2009.
- [23] M. G. Villalva, T. G. de Siqueira, and E. Ruppert, "Voltage regulation of photovoltaic arrays: small-signal analysis and control design," *IET Power Electronics*, vol. 3, Issue. 6, pp. 869-880, 2010.
- [24] C. Li, Y. Chen, D. Zhou, J. Liu, and J. Zeng, "A high-performance adaptive incremental conductance MPPT algorithm for photovoltaic systems," *Energies*, vol. 9, no. 4, Apr. 2016.
- [25] A. Morales-Acevedo, J. L. Díaz-Bernabé and R. Garrido-Moctezuma, "Improved MPPT Adaptive Incremental Conductance Algorithm," *Proc. IEEE IECON2014*, pp. 5540-5545, 2014.
- [26] "Setting the P-I Controller Parameters, KP and KI", Appl. Note. TLE7242 and TLE8242, Infineon Technologies AG, Germany, Oct. 2009.
- [27] Mohan, N., Robbins, W. and Undeland, T., "Power electronics Converters Applications and Design 3rd ed", NJ: Wiley, 2003, Page 172-174.
- [28] Li. Tan., "Digital Signal Processing Fundamental and Applications", Elsevier: Academic Press, 2008, Page 557-559.
- [29] H. F. Blanchette, T. Ould-Bachir and J. P. David, "A State-Space Modeling Approach for the FPGA-Based Real-Time Simulation of High Switching Frequency Power Converters," *IEEE Trans. Ind. Electron.*, vol. 59, no. 12, pp. 4555-4567, Dec. 2012.



**Mandip Pokharel** (S'16) received his B.Eng. in Electrical and Electronics from Kathmandu University, Nepal in 2008 and M.Eng. degree jointly from Norwegian University of Science and Technology (NTNU), Norway and Kathmandu University (KU), Nepal under NORAD fellowship in 2012. Currently, he is at University of Manitoba, Canada working towards his PhD degree.

Before joining University of Manitoba, he worked as a design and project engineer in various transmission line and substation-based projects. His research interest includes Control

System for Power Electronic applications, Renewable energy, Solar and Wind Emulators, Real Time Simulations and Power Hardware in the Loop simulations.



**Avishek Ghosh** (S'18) received the B.Eng. degree in Electronics and Electrical Engineering with first class honours from the University of Glasgow, UK in 2012. He has worked in the Energy sector in India from 2012 to 2016. As a Project Engineer, he gained industrial experience in areas of manufacturing, testing and commissioning of Electrostatic Precipitator (ESP) technologies, HV Switchgears, and other substation equipment. He is currently pursuing M.Sc. degree in the department of Electrical and Computer Engineering and working as a Research Assistant at the Renewable-energy Interface and Grid Automation (RIGA) Lab in the University of Manitoba, Winnipeg, Canada.

His current research interests include Wide-bandgap semiconductor device characterization and applications.



**Carl Ngai Man Ho** (M'07, SM'12) received the B.Eng. and M.Eng. double degrees and the Ph.D. degree in electronic engineering from the City University of Hong Kong, Kowloon, Hong Kong, in 2002 and 2007, respectively.

From 2002 to 2003, he was a Research Assistant at the City University of Hong Kong. From 2003 to 2005, he was an Engineer at e.Energy Technology Ltd., Hong Kong. In 2007, he joined ABB Switzerland. He has been appointed as Scientist, Principal Scientist, Global Intellectual Property Coordinator and R&D Principal Engineer. He

has led a research project team at ABB to develop Solar Inverter technologies. In October 2014, he joined the University of Manitoba in Canada as Assistant Professor and Canada Research Chair in Efficient Utilization of Electric Power. He established the Renewable-energy Interface and Grid Automation (RIGA) Lab at the University of Manitoba to research on Microgrid technologies, Renewable Energy interfaces, Real Time Digital Simulation technologies and demand side control methodologies.

Dr. Ho is currently an Associate Editor of the IEEE Transactions on Power Electronics (TPEL) and the IEEE Journal of Emerging and Selected Topics in Power Electronics (JESTPE). He received the Best Associate Editor Award of JESTPE in 2018.